



HiFi-Syn: Hierarchical Granularity Discrimination for High-Fidelity Synthesis of MR Images with Structure Preservation

Ziqi Yu^{a,b}, Botao Zhao^c, Shengjie Zhang^{a,b}, Xiang Chen^{a,b}, Jianfeng Feng^{a,b}, Tingying Peng^{d,*}, Xiao-Yong Zhang^{a,b,*}

^aInstitute of Science and Technology for Brain-Inspired Intelligence, Fudan University, Shanghai, 200433, China

^bMOE Key Laboratory of Computational Neuroscience and Brain-Inspired Intelligence, and MOE Frontiers Center for Brain Science, Fudan University, Shanghai, 200433, China

^cResearch Center for Augmented Intelligence, Zhejiang Lab, Hangzhou, 311121, China

^dHelmholtz AI, Helmholtz zentrum Muenchen, Munich, D-85764, Germany

ARTICLE INFO

Article history:

Keywords:

Medical image synthesis
Brain MRI
Structure preservation
Hierarchical granularity
Disentangled representations

ABSTRACT

Synthesizing medical images while preserving their structural information is crucial in medical research. In such scenarios, the preservation of anatomical content becomes especially important. Although recent advances have been made by incorporating instance-level information to guide translation, these methods overlook the spatial coherence of structural-level representation and the anatomical invariance of content during translation. To address these issues, we introduce hierarchical granularity discrimination, which exploits various levels of semantic information present in medical images. Our strategy utilizes three levels of discrimination granularity: pixel-level discrimination using a Brain Memory Bank, structure-level discrimination on each brain structure with a re-weighting strategy to focus on hard samples, and global-level discrimination to ensure anatomical consistency during translation. The image translation performance of our strategy has been evaluated on three independent datasets (UK Biobank, IXI, and BraTS 2018), and it has outperformed state-of-the-art algorithms. Particularly, our model excels not only in synthesizing normal structures but also in handling abnormal (pathological) structures, such as brain tumors, despite the variations in contrast observed across different imaging modalities due to their pathological characteristics. The diagnostic value of synthesized MR images containing brain tumors has been evaluated by radiologists. This indicates that our model may offer an alternative solution in scenarios where specific MR modalities of patients are unavailable. Extensive experiments further demonstrate the versatility of our method, providing unique insights into medical image translation.

© 2023 Elsevier B. V. All rights reserved.

1. Introduction

In recent years, unsupervised Image-to-Image (I2I) translation has made significant progress, emerging as a promis-

ing solution for medical image synthesis in various scenarios, such as generating missing images and predicting disease outcomes (Lee et al., 2021; Ma et al., 2021). Obtaining large-scale, multi-modal magnetic resonance imaging (MRI) data is often costly and, in some cases, even impractical due to factors such as patient cooperation and medical data privacy. As an alternative, synthesizing new MRI data can provide complementary

*Corresponding author: xiaoyong_zhang@fudan.edu.cn; tingying.peng@tum.de

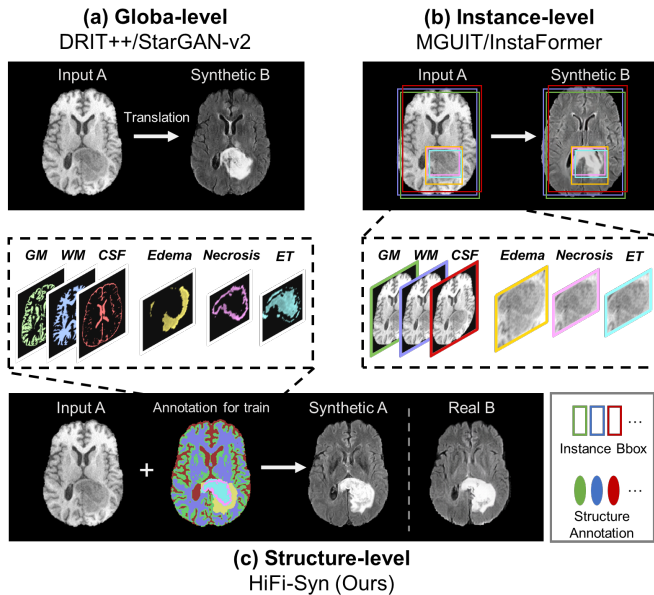


Fig. 1. Illustration of our motivation. Current Image-to-Image (I2I) methods, both (a) global-level and (b) instance-level, often overlook the spatial coherence of structural-level representation and the anatomical consistency of content during translation. To address this limitation, we introduce a (c) structure-level content translation method for synthesizing MR images containing both normal and abnormal tissues.

information regarding tissue morphology. Like natural image synthesis, cycle-consistent generative adversarial network (CycleGAN) (Zhu et al., 2017) and its variants are the primary approaches for synthesizing medical images. The quality of the synthesized images is often assessed by two evaluation metrics: 1) global-level measures such as Peak Signal to Noise Ratio (PSNR); and 2) patch-level measures such as Structural Similarity Index (SSIM) and MS-SSIM.

In most medical image synthesis tasks, the primary requirement is translation in a *structure-preserving* manner. This is crucial for dependable downstream analyses and applications. Unfortunately, this requirement has not been sufficiently addressed or reflected in previous methods and evaluation metrics. Take, for example, the synthesis of brain MRI images. The resulting brain MRIs must maintain the appearance inherent to the target modality on a global scale, while also preserving the anatomical structure of the source image at a local level. Moreover, synthesizing pathological structures is of equal importance as normal anatomical structures. For instance, in T1-MRI scans, conditions like edema or brain tumors often appear as regions of decreased signal intensity. In contrast, elevated signal regions might indicate intracranial hemorrhage (Saini et al., 2019).

In T2-MRI, these pathological structures may show opposite contrast distribution, with higher signals for brain tumors, and lower signals for hemorrhage. In such scenarios, GANs are tasked with identifying the subset of pixels at the structural level for translation, which we refer to as *structure-preserving translation*. However, most existing networks only model holistic contrast shifting, which aims for global-level reconstruction without the consideration of local-level structures or contexts.

For example, existing GANs often struggle with accurately translating the signal intensity of tumors and lesions across various modalities. Moreover, these structure-wise signal changes aren't adequately captured by current metrics, compounding the challenge and more comprehensive evaluations are needed to assess the model's real capabilities.

Recently, there have been several efforts to exploit local object information in instance-level I2I translation (Shen et al., 2019; Jeong et al., 2021; Kim et al., 2022). INIT (Shen et al., 2019) utilises a reconstruction loss in conjunction with the global translation module to independently translate the instances during training. As for testing, the model only employs the global module and neglects the instance-level details. This might lead to unexpected performance deterioration in practice. MGUIT (Jeong et al., 2021) proposes using an external memory module to store the style features for each category. However, the lack of structural and global-level guidance may lead to fragmented representations in the embedding content space. The anatomical content may also alter during translation since the training procedure has no explicit supervision. To obtain richer instance features, InstaFormer (Kim et al., 2022) additionally uses patches of each instance for representation learning, yet their bounding-box annotations are too coarse to capture the fine brain structures. Furthermore, in medical images, different structures are usually highly intertwined - for example, as shown in Fig. 1, one can refer to MR images to observe the existence of gyri and sulci, which are located on the surface of the brain in the gray matter (GM) and white matter (WM) regions. Thus, it poses challenges for the network design.

Motivated by the aforementioned issues, we aim to propose a *structure-preserving* medical image-to-image translation model. Specifically, we design a disentangled and contrastive GAN-based framework that uses hierarchical granularity discrimination to exploit various level of semantic information in medical images. First, we introduce pixel-level granularity discrimination using a Brain Memory Bank (BMB). To make the memory items more discriminative and the memory space more compact, we impose constraints on them to make similar items closer and push dissimilar items away. Second, to make the translation structure-aware, we employ structure-level granularity discrimination on each brain structure, with a re-weighting strategy to allow the network to focus on hard samples. Finally, we utilize global-level granularity discrimination to ensure the consistency of anatomical content during translation. Our experiments on three public datasets, BraTS (Menze et al., 2014), IXI¹, and UKB (Miller et al., 2016), demonstrate the superiority of our proposed framework by showcasing its ability to maintain the integrity of normal brain structures while faithfully reconstructing pathological lesions. More importantly, beyond PSNR and SSIM, we perform quantitative evaluations on related downstream tasks such as voxel-level analysis. In addition, medical experts are involved to check our generated images visually, demonstrating that our method consistently preserves the structures during image translation.

Our contributions can be summarized as follows:

¹<https://brain-development.org/ixi-dataset/>

- We propose a novel medical image-to-image translation framework designed to preserve both normal and pathological (abnormal) structural information during the translation process.
- Our proposed framework employs a disentangled and contrastive GAN-based approach that utilizes hierarchical granularity discrimination to exploit various levels of semantic information in medical images.
- We conduct extensive experiments and voxel-level evaluations on three datasets, encompassing various modalities (T1, T1ce, T2, and T2-Flair) and tasks (normal tissue and tumor). The results demonstrate the robustness of our model, outperforming previous state-of-the-art algorithms, and showcase the effectiveness of our approach in practical downstream applications, including the preservation of diagnostic value and segmentation tasks.

2. Related work

2.1. Image-to-Image Translation

Generative adversarial networks and their derivatives have been extensively utilized in the I2I translation tasks. Among the most seminal papers is Pix2Pix (Isola et al., 2017), which harnessed paired images through conditional generative adversarial networks, yielding remarkable results in image-to-image translation tasks. As the collection of paired data can usually be costly and impractical, prompting the development of numerous unsupervised I2I translation algorithms. Following the success of CycleGAN (Zhu et al., 2017), which used the cycle-consistency constraint for training the network, substantial attempts have been made on construction strategies for encoder and decoder, such as DiscoGAN (Kim et al., 2017) and DualGAN (Yi et al., 2017). In order to generate multiple domain outputs, MUNIT (Huang et al., 2018), DRIT++ (Lee et al., 2020), and StarGAN-v2 (Choi et al., 2020) were proposed. There are many efforts to deploy such algorithms in medical images, involving modalities such as MRI, CT, and PET (Özbey et al., 2023; Dalmaz et al., 2022; Yu et al., 2021, 2022b; Chartsias et al., 2019a,b). However, most of them only consider global-level information during translation, which may lead to unsatisfied performance when addressing images within multiple objects, such as organs or structures.

2.2. Instance-level Image-to-Image Translation

To achieve instance-aware I2I translation, several attempts (Shen et al., 2019; Jeong et al., 2021; Kim et al., 2022) have been exploited in recent years. INIT (Shen et al., 2019) was used to translate the entire image and instances independently. However, in the test phase, it discarded the instance-level information. DUNIT (Bhattacharjee et al., 2020) was proposed to employ instance consistency loss for object-awareness and further train the computationally expensive detection module, which made it inflexible. MGUIT (Jeong et al., 2021) employs bounding boxes to read and write a memory module for storing class-aware features. Contrastive representation (Zhang et al., 2023; Yu et al., 2023) serves as one of foundational concept in

InstaFormer (Kim et al., 2022), which incorporating patch-level contrasts within a Transformer-based network, drawing inspiration from the approach introduced by (Park et al., 2020b).

However, the aforementioned methods have inherent limitations. For instance, coarse bounding boxes may struggle to accurately indicate instances when they are overlapped or have irregular shapes. Additionally, retrieving the memory module solely through pixel-level queries neglects their region-wise spatial relationship. Unfortunately, these concerns become even more serious when dealing with medical images.

2.3. Structure-Preserving Translation

In the field of medical image translation, few studies introduced structural consistency to improve the synthesis of more realistic images. Hiasa et al. proposed GC-CycleGAN (Hiasa et al., 2018) to generate corresponding pelvis CT from MRI. They introduced gradient consistency loss in CycleGAN to improve the accuracy at the boundaries. Yang et al. introduced SC-CycleGAN (Yang et al., 2020) for unsupervised MR-to-CT synthesis, emphasizing structural consistency using a modality-independent neighborhood descriptor in the structure-consistency loss. Their primary focus is MRI-to-CT synthesis. While CT captures brain exterior and cranial bone structures, it lacks internal brain details crucial for neuroscience analysis.

In recent studies, mutual information loss (Kang et al., 2023) has been introduced to maintain content consistency, and outer contours of the brain (Phan et al., 2023) and organs (Emami et al., 2021) have been utilized for shape consistency. However, the dependency on implicit loss or coarse shape consistency in the mentioned approaches may present challenges, particularly when handling multi-contrast MRI images. The intricate details and variations in contrast levels across different MRI sequences demand a more nuanced and adaptable approach to ensure effective structural preservation. Taking these considerations into account, we propose a model that incorporates constraints based on brain region structures. This tailored approach not only enhances structural consistency but also ensures adaptability to the diverse discrepancies within different MRI sequences.

2.4. Disentangled Representation for Multiple Discrimination

GAN brings strong disentanglement prior because of its hierarchical structure (Kwon and Ye, 2021; Locatello et al., 2019a), which naturally fits our purpose. To further promote this progress, we utilize contrastive learning (Khosla et al., 2020a) in different level discrimination to improve existing methods.

Memory network (Weston et al., 2014) maintains a collection of feature vectors extracted from the input data. These feature vectors can be accessed by a set of queries. Many derivatives of memory modules have been proposed (Park et al., 2020a; Gong et al., 2019; Jeong et al., 2021), however, similar to MGUIT (Jeong et al., 2021), most of them mainly consider pixel-level representations. To enrich the spatial coherence of learned embedding space, we incorporate structure-wise and global-level discrimination inspired from (Hu et al., 2021). Combined with the characteristics of medical imaging data, we also impose contrastive loss (Khosla et al., 2020a) at subject-level for *structure-preserving* translation.

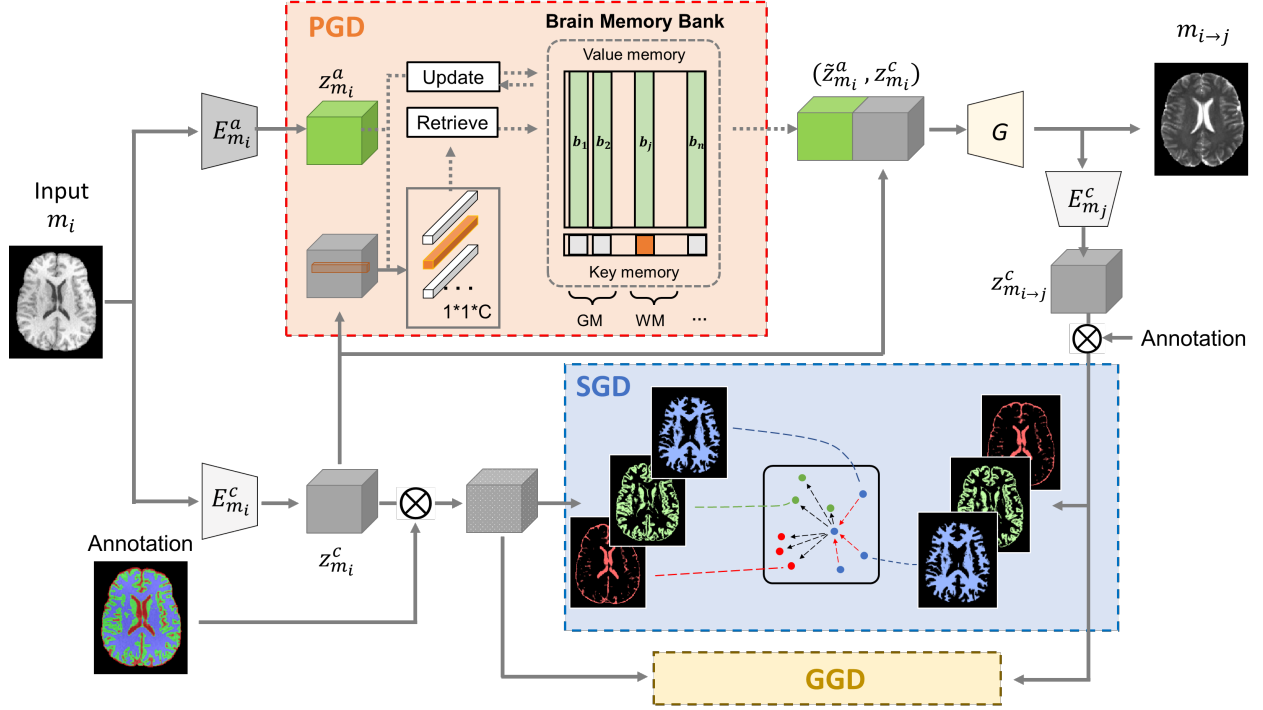


Fig. 2. The overview of our proposed framework. The input images are encoded to content and attribute features and then processed by Pixel-level Granularity Discrimination (PGD) module, Structure-level Granularity Discrimination (SGD) module, and Global-level Granularity Discrimination (GGD) module simultaneously to achieve structure-preserving translation. Note that the annotations are unseen during testing. For the sake of conciseness, the second-stage style translation is not illustrated here.

3. Methods

3.1. Inductive Bias of Disentanglement

Unsupervised disentanglement is considered impossible without the imposition of appropriate inductive biases (Locatello et al., 2019a). In light of this, we introduce our basic assumption that medical images can be decoupled into content and attribute factors, where content factors should solely capture anatomical structural information while attribute factors should focus only on image appearance. We argue that this assumption aligns well with the fundamental nature of multi-modality MRIs. To this end, we describe how we embed semantic image features to modality-specific attribute space and modality-independent content space in this subsection. We will further explore this assumption for I2I translation in the subsequent sections.

Considering we have K number of modalities in the dataset and $\{M_i\}_{i=1}^K$ denotes each modality. m_i presents each sampled image from corresponding modality. We adopt the architecture of DRIT++ (Lee et al., 2020) as our backbone network following its success. Therefore, we omit unnecessary details to avoid repetition. In summary, our translation model includes two content encoders $E_{m_i}^c, E_{m_j}^c$, attribute encoders $E_{m_i}^a, E_{m_j}^a$, generators G_{m_i}, G_{m_j} , and modality discriminators D_{m_i}, D_{m_j} . Given input images $\{m_i, m_j\}$, the first forward image style translation, we obtain encoded content features $\{z_{m_i}^c, z_{m_j}^c\} = \{E_{m_i}^c(m_i), E_{m_j}^c(m_j)\}$, and attribute features $\{z_{m_i}^a, z_{m_j}^a\} = \{E_{m_i}^a(m_i), E_{m_j}^a(m_j)\}$ as well as the translated pair of images $m_{i \rightarrow j}, m_{j \rightarrow i}$. Similarly, in the second style translation,

we acquire features $\{z_{m_{i \rightarrow j}}^c, z_{m_{j \rightarrow i}}^c, z_{m_{i \rightarrow j}}^a, z_{m_{j \rightarrow i}}^a\}$ and reconstructed images $\{\hat{m}_i, \hat{m}_j\}$ from these synthesized images. In this way, we can achieve vanilla disentanglement, yet we note that this disentanglement only takes global information into account. In the next section, we describe how we promote structure-aware disengagement via triple-level granularity discrimination.

3.2. Structure-preserved Translation

3.2.1. Pixel-level Granularity Discrimination (PGD)

To ensure that the translation procedure is structure-invariant, we first introduce pixel-level granularity discrimination into our framework. Unlike the instance-granularity mechanism that treats each image as a separate entity, thus limiting in modelling a relatively global discriminative feature representation, our pixel-level granularity regards each pixel in the content encoder E^c as an individual candidate, hence allowing for dense semantic distinct feature representations. Besides, we establish Brain Memory Bank (BMB) to keep track of these feature representations. The BMB is designed as $B \in \mathbb{R}^{N \times C}$ including N slots to store value vectors with the dimension C . In each slot b_i^k , which stands for a i_{th} memory item of category k , is to store domain-specific attribute representations, and key is used as an address for retrieving relevant memory items. During the training procedure, we first retrieve the BMB and obtain enhanced domain-agnostic features $\hat{z}_{m_i}^a$ by using query map, i.e. the content codes $z_{m_i}^c$, and then channel-wise combining the input attribute features $z_{m_i}^a$ with the retrieved ones $\hat{z}_{m_i}^a$ for subsequent domain translation.

Note that, in contrast to existing memory bank techniques that only consider the content codes from the original images (Jeong et al., 2021), we impose contrastive consistency to consider contents of original and translated images $\{q_{m_i}^{n,k}, q_{m_{i \rightarrow j}}^{n,k}\}$ as positive samples, thus keeping the structural information invariant at pixel-level during translation.

Retrieving. Given the content feature $z_{m_i}^c = E_{m_i}^c(m_i)$ of size $H \times W \times C$, where H, W, C stand for height, width, and the channel number, respectively. We define the set of pixel-wise queries $\{q_{m_i}^n\}_{n=1}^N \in \mathbb{R}^c$, where $N = H \times W$ and each query has the size of $1 \times 1 \times C$. Then, we can use softmax operation to obtain affinity scores $w_i^{n,k}$ for each category:

$$w_i^{n,k} = \frac{\exp(\text{sim}(q_{m_i}^n, k^n))}{\sum_{j=1}^N \exp(\text{sim}(q_{m_i}^n, k^n))}, \quad (1)$$

where $\text{sim}(\cdot, \cdot)$ denotes cosine similarity:

$$\text{sim}(q_{m_i}^n, k^n) = \frac{q_{m_i}^n \cdot k^n}{\|q_{m_i}^n\|_2 \|k^n\|_2}. \quad (2)$$

To get the enhanced representation, $\tilde{z}_{m_i}^a$, the memory module retrieves the memory elements that are close to $z_{m_i}^a$. This procedure can be defined as follows:

$$\tilde{z}_{m_i}^a = \sum_{i=1}^N w_i \cdot z_{m_i}^a, \quad (3)$$

Updating. For updating memory items, we choose all queries that identify the item as the close ones for each b_i using the affinity scores in (1) and obtain updating weight $u_{m_i}^k$. Then we update the keys and values in BMB through:

$$\tilde{\mathcal{K}} \leftarrow \|\alpha_p \cdot \mathcal{K} + (1 - \alpha_p) \cdot \sum_{n'=1}^N u_{m_i}^k \cdot (q_{m_i}^{n'} + q_{m_j}^{n'})\|_2. \quad (4)$$

$$\tilde{b}_{m_i} \leftarrow \|\alpha_p \cdot b_{m_i} + (1 - \alpha_p) \cdot \sum_{n'=1}^N u_{m_i}^k \cdot \tilde{z}_{m_i}^a[n']\|_2. \quad (5)$$

$$u_{m_i}^k = \frac{\exp(\text{sim}(q_{m_i}^n, k^n))}{\sum_{j=1}^N \exp(\text{sim}(q_{m_i}^n, k^n))}, \quad (6)$$

where α_p is to control updating rate. Similarly, we can compute $\tilde{b}_{m_j}^n$ for items stored attributes from other domains.

To promote learning a better-disentangled feature representation, we introduce a contrastive prior here for each specific subject, the content features of input image m_i and translated images $m_{i \rightarrow j}$ are close to each other in latent content space since they share the same intrinsic structures (positive pairs, Ω_p^+). In contrast, images of different subjects (even if they belong to the same modality) are pushed away. Based on this assumption, we impose pixel-level contrastive loss, which could be formulated as follows:

$$\mathcal{L}_{PGD} = \sum_{i=1}^N \frac{-1}{|\Omega_p^+|} \sum_{m^+ \in \Omega_p^+} \log \frac{\exp(CL^+/\tau_1)}{\sum_{m \in \Omega_p} \exp(CL/\tau_1)} \quad (7)$$

where $CL^+ = \text{sim}(q_{m_i}^n, q_{m^+}^n)$, $CL = \text{sim}(q_{m_i}^n, q_m^n)$ and $\Omega_p^+ = \Omega_p / \{q_{m_i}^n\}$. τ_1 is the temperature scaling parameter.

3.2.2. Structure-level Granularity Discrimination (SGD)

In the above pixel-level granularity discrimination module, each pixel in the content space is treated independently of the other. Here we go one step further to explore structure-level granularity discrimination (SGD), thereby calibrating the deformation of structural semantic content during translation. By leveraging available training data with annotated brain structures, SGD can learn decoupled features at the structure-level, thus capturing more characteristic variations between different anatomical structures in the brain. We show in our experiments later that SGD is a critical intermediate component that leads to more efficient and robustness learning than existing methods, either learning from the pixel-level or global level.

Similarly, we use contrastive learning in SGD to pull region semantic features of the same structures together while keeping features of different structures apart. Thereby, we reuse the disentangled content features $z_{m_i} \in \mathbb{R}^{H \times W \times C}$ and annotated structural ground truth $G_{m_i} \in \mathbb{R}^{H \times W}$ which are down-sampled to the H, W matrix size. Denoting L as the number of structures $\{s\}_{i=1}^L$, with the guidance of G_{m_i} , we can obtain structure-wise content $z_{m_i}^{c,s_i}$ of modality M_i via:

$$z_{m_i}^{c,s_i} = z_{m_i}(x, y) \odot \mathbb{1}[G_{m_i}(x, y) = s_i] \quad (8)$$

where \odot presents Hadamard product and (x, y) is position coordinate. $\mathbb{1}(\cdot)$ is the binary indicator denoting whether the pixel belongs to s_i . Similarly, we have translated $z_{m_{i \rightarrow j}}^{c,s_i}$ of modality $M_{i \rightarrow j}$. Though they can be assigned to diverse appearance conditioned by different attribute codes, the anatomical content of $\{z_{m_i}^{c,s_i}, z_{m_{i \rightarrow j}}^{c,s_i}\}$ from the same subject ought to be accordant which belongs to positive samples $\{z_{m^+}^{c,s_i}\} \in \Omega_s^+$. Negative samples Ω_s^- include residual structures and anatomical content features from other subjects. Moreover, to force the network to pay more attention to hard examples, we design a content similarity-based weighting scheme to automatically adjust weights for each sample. Specifically, given a set of structures $\{s\}$ from one subject regardless of the modality, the deformation maps $\{d_{s_i}\}$ guide the weight between each two positive samples, and the ranking-based weighting calculation can be defined as:

$$d_{s_i} = \sum_{x,y} |z_{m_i}^{c,s_i} - z_{m_{i \rightarrow j}}^{c,s_i}| \quad (9)$$

$$w_{s_i} = \exp(-\alpha_s \cdot \text{rank}(d_{s_i})) \quad (10)$$

where hyper-parameter α_s controls the degree of smoothness in the exponential function, and $\text{rank}(\cdot)$ involves sorting the values in a set. w_{s_i} varies from 0 to 1. Pairs with greater deformation are accorded larger weights. It can harness the network to correct mismatches, thereby preserving the brain structure during the style translation. Finally, the overall loss for structure-level granularity discrimination can be defined as follows:

$$\mathcal{L}_{SGD} = \sum_{i=1}^N \frac{-1}{|\Omega_s^+|} \sum_{m^+ \in \Omega_s^+} \log \frac{\exp(w_{s_i} \cdot CL^+/\tau_2)}{\sum_{m \in \Omega_s} \exp(CL/\tau_2)} \quad (11)$$

where $CL^+ = \text{sim}(z_{m_i}^{c,s_i}, z_{m^+}^{c,s_i})$, $CL = \text{sim}(z_{m_i}^{c,s_i}, z_m^{c,s_i})$, $m^+ \in \Omega_s^+$, and $\Omega_s^+ = \Omega_s / \{s_i\}$. τ_2 is the temperature scaling parameter

3.2.3. Global-level Granularity Discrimination (GGD)

To mitigate the decline in performance during the test phase when structural annotations are not accessible, we further introduce a global-level granularity discrimination (GGD) here, by adding a set of global-level memory items to BMB. The integration of GGD into BMB is seamless and can be implemented similarly to PGD, as described in Section 3.2.1. For symmetry, the number of entity items belonging to GGD is equal to the sum of those in PGD.

Similar to the previous SGD, the global anatomical content from the same entity should remain consistent, regardless of the target modalities to which it is translated. To achieve this, we leverage the entire content feature $z_{m_i}^c$ and apply contrastive learning loss, which is similar to the equation (11) but with $w_{s_i} = 1$. For the sake of avoiding redundancy, we refrain from restating the formulation here.

3.3. The Overall Loss Function

The full loss function of our framework is:

$$\min_{(E^c, E^a, G)} \max_{(D, D^c)} \mathcal{L}(E^c, E^a, G) = \lambda_1 \mathcal{L}_{adv}^{cont} + \lambda_2 \mathcal{L}_{adv}^{domain} + \lambda_3 \mathcal{L}_1^{cyc} + \lambda_4 \mathcal{L}_1^{self-recon} + \lambda_5 \mathcal{L}_{PGD} + \lambda_6 \mathcal{L}_{SGD} + \lambda_7 \mathcal{L}_{GGD} \quad (12)$$

Besides the loss terms we explained in PGD, SGD and GGD, we also have $\{\mathcal{L}_1^{cyc}, \mathcal{L}_1^{self}, \mathcal{L}_{adv}^{cont}, \mathcal{L}_{adv}^{domain}\}$, similar to DRIT++ (Lee et al., 2020).

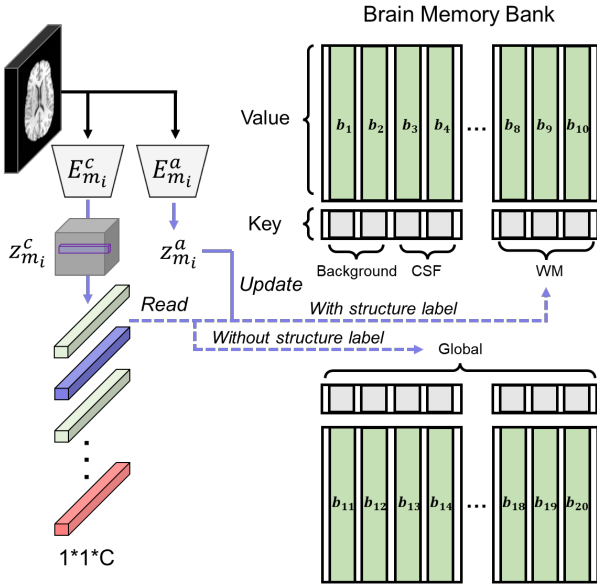


Fig. 3. Illustration of memory item setting for the IXI/UKB datasets. Each query reads and updates the corresponding structure-aware items with labels and global items without labels during training. Items store domain-specific attribute representations, utilizing shared keys to access them.

4. Experimental Setup

4.1. Datasets

We conducted experiments on three widely recognized public datasets of brain MRIs.

4.1.1. BraTS Dataset

The 2018 Multimodal Brain Tumor Segmentation Challenge (BraTS) dataset (Menze et al., 2014) consists of 285 annotated MRI subjects from glioma patients across multi-institution. Each subject has four aligned modalities, T1, T1ce, T2, and FLAIR. The MRI volumes had been skull-stripped and re-sampled to the resolution of $1 \times 1 \times 1 \text{ mm}^3$. We used 100 subjects for I2I translation, where 70 are reserved for training and 30 are for testing. From each subject, 100 axial cross-sections containing brain tissues are selected. This dataset contains 3 classes of tumor labels (core, enhancing, and whole tumor) initially. Further, we invite two expert radiologists to delineate and curate the segmentation of gray matter (GM), white matter (WM), and cerebrospinal fluid (CSF) using FSL (Jenkinson et al., 2012) and itk-snap (Yushkevich et al., 2016). Finally, we have six classes in total, which include GM, WM, and CSF, as well as edema, necrosis, and enhancing tumor regions.

4.1.2. IXI Dataset

In IXI dataset, T1 and T2 brain MR images from 80 healthy subjects are used in our study, where 60 are reserved for training and 20 for testing. Like in BraTS, we also select 100 axial cross-sections containing brain tissues for IXI dataset. However, no segmentation labels were provided in this dataset. Therefore, we ask two expert radiologists to provide us with three classes of GM, WM, and CSF, with the assistance of FSL (Jenkinson et al., 2012) and itk-snap (Yushkevich et al., 2016).

4.1.3. UKB Dataset

This dataset comprises MR images sourced from UK Biobank (Miller et al., 2016). In our study, we employed T1 and T2-Flair MRI images from 100 healthy subjects, with 70 individuals allocated for training and 30 for testing. Consistent with the setting for the BraTS and IXI datasets, we select 100 axial cross-sections containing brain tissues for our analysis and obtain structural labels in this dataset with those criteria used in the IXI dataset. Incorporating the UKB dataset into our study enhances the diversity and comprehensiveness of our datasets and experiments, as it encompasses a broader spectrum of subjects and imaging scenarios commonly encountered in real-world clinical practice.

4.2. Implementation Details

Our model is implemented using Pytorch (Imambi et al., 2021), building upon the implementation of DRIT++ (Lee et al., 2018), and trained on one NVIDIA Tesla V100 GPU. Input images are resized to 256×256 matrix size and are normalized to the range of $[-1, 1]$. We use Adam optimizer with a learning rate of 0.0001, and set the size of the batch to 2. We set the content features $z_{m_i}^c$ with height H , weight W , and feature channel number C to 54, 54, and 256, respectively.

The Brain Memory Bank (BMB) is divided into two distinct parts. The items belonging to the pixel-level granularity discrimination (PGD) module solely focus on structural-wise knowledge, whereas the remaining items encompass global-level information, attributed to global-level granularity discrimination (GGD). Empirically, these two parts are symmetrical in

Table 1. Quantitative evaluation on the IXI dataset. We perform bidirectional translation for each domain pair and evaluate the performance using PSNR and SSIM metrics, where higher values indicate better results

	CycleGAN		GC-CycleGAN		SC-CycleGAN		MUNIT		DRIT++		StarGAN-v2		MGUIT		InstaFormer		HiFi-Syn	
	PSNR	SSIM	PSNR	SSIM	PSNR	SSIM	PSNR	SSIM	PSNR	SSIM	PSNR	SSIM	PSNR	SSIM	PSNR	SSIM	PSNR	SSIM
T1→T2	19.7149	0.7739	19.7751	0.7762	20.6816	0.7852	20.9800	0.7833	22.3210	0.8050	22.1558	0.7975	24.3749	0.7949	22.3974	0.8108	23.8376	0.8240
T2→T1	20.3284	0.7862	20.3541	0.7914	20.4581	0.8003	21.7122	0.8024	22.2411	0.7722	22.5482	0.8131	23.2653	0.8231	22.8315	0.8259	24.1751	0.8371
Average	20.0217	0.7801	20.0646	0.7838	20.5699	0.7928	21.3461	0.7929	22.2810	0.7886	23.3520	0.7975	23.8201	0.8090	22.6145	0.8184	24.0064	0.8306

Table 2. Quantitative evaluation on the UKB dataset. We perform bidirectional translation for each domain pair and evaluate the performance using PSNR and SSIM metrics, where higher values indicate better results

	CycleGAN		GC-CycleGAN		SC-CycleGAN		MUNIT		DRIT++		StarGAN-v2		MGUIT		InstaFormer		HiFi-Syn	
	PSNR	SSIM	PSNR	SSIM	PSNR	SSIM	PSNR	SSIM	PSNR	SSIM	PSNR	SSIM	PSNR	SSIM	PSNR	SSIM	PSNR	SSIM
T1→T2-Flair	21.8037	0.7404	21.8138	0.7527	22.0411	0.7648	22.3803	0.8074	22.4867	0.8115	22.9423	0.8158	23.2816	0.8279	23.1576	0.8290	23.3611	0.8337
T2-Flair→T1	22.2846	0.7718	22.4855	0.7864	22.5284	0.7903	23.4913	0.8106	23.3427	0.8261	23.7714	0.8305	24.5478	0.8351	25.0543	0.8372	24.9759	0.8459
Average	22.0442	0.7561	22.1497	0.7696	22.2848	0.7776	22.9358	0.8090	22.9147	0.8188	23.3569	0.8232	23.9147	0.8315	24.1060	0.8331	24.1685	0.8398

size, each containing an equal number of items. In accordance with this symmetrical configuration, the number of memory items for the IXI/UKB dataset is set to 20, while for the BraTS dataset, it is set to 38 items. In instance, for the IXI dataset, the 20 memory items are divided into 2 for the background, 2 for CSF, 3 for GM, 3 for WM, and 10 for global structures. The diagram is presented in Fig. 3. In contrast to MGUIT (Jeong et al., 2021), we employ structure-wise annotations instead of bounding boxes to locate pixel positions, resulting in more precise structural descriptions. Additionally, we introduce items to record global values in the BMB, recognizing that annotations are not available during the testing phase. We expect the network to learn contextual discrepancies from the input rather than solely relying on labels, thereby ensuring the robustness and generalizability of the network.

The hyperparameter $\{\lambda_{1-4}\}$ are set the same as DRIT++ (Lee et al., 2020). Empirically, we set $\alpha_p = 0.01$, $\alpha_s = 0.5$, $\lambda_5, \lambda_7 = 1$, and $\lambda_6 = 2$.

4.3. Evaluation Metrics

We trained all I2I translation networks in an unpaired manner and evaluated their performance using the Peak Signal Noise Rate (PSNR) and Structural Similarity Index Measure (SSIM). Note that raw images from the IXI dataset are unregistered, so we employed BEN (Yu et al., 2022a) and ANTs (Avants et al., 2009) to register them at subject-level after skull-stripping to get real reference images for evaluating I2I translation performance on the IXI dataset.

In addition to PSNR and SSIM, we incorporated the Dice score and volumetric similarity metrics to evaluate the anatomical-level quality of image translation. By focusing on segmented structures of interest, we are able to achieve a more reliable and comprehensive measurement of structural fidelity during image synthesis.

4.4. Competitive Methods

We compare our proposed framework with unsupervised image-to-image translation methods, including CycleGAN (Zhu et al., 2017), MUNIT (Huang et al., 2018), StarGAN-v2 (Choi et al., 2020), DRIT++ (Lee et al., 2020), as well as the recently state-of-the-art (SOTA) instance-level I2I methods MGUIT (Jeong et al., 2021) and InstaFormer (Kim et al., 2022). In addition, we also include two medical structure-constrained

translation methods, GC-CycleGAN (Hiasa et al., 2018) and SC-CycleGAN (Yang et al., 2020), to demonstrate the effectiveness of our proposed methods.

- **CycleGAN:** A classic unsupervised image-to-image translation method that has been widely adopted in various domains. It employs a cycle-consistency loss to ensure consistency between the translated and original images in both directions, contributing to improved image quality and preservation of content.
- **MUNIT:** MUNIT focuses on multimodal translation tasks, aiming to generate diverse outputs from a single input image. It introduces disentangled representations for content and style, enabling more flexible and controlled image synthesis across different domains.
- **StarGAN-v2:** StarGAN-v2 extends the capabilities of its predecessor by enabling image translation across multiple domains with a single model. It introduces a novel method for learning domain-specific style codes, resulting in improved image quality and diversity in the translated outputs.
- **DRIT++:** DRIT++ builds upon the disentangled representation framework, aiming for diverse image translation. It introduces additional enhancements to improve the diversity and quality of the generated images while maintaining disentanglement for better control over the translation process.
- **MGUIT:** It introduces a memory mechanism to store and utilize relevant information during the translation process. By incorporating memory guidance, MGUIT aims to enhance the model's ability to generate accurate and contextually relevant translations.
- **InstaFormer:** InstaFormer is a recent state-of-the-art instance-level image-to-image translation method. It leverages a transformer-based architecture to capture long-range dependencies and context information, enhancing the model's ability to generate realistic and coherent translations at the instance level.
- **GC-CycleGAN:** It introduces a gradient consistency loss into the traditional CycleGAN architecture. The gradient

Table 3. Quantitative evaluation on the BraTS dataset. We perform bidirectional translation for each domain pair and evaluate the performance using PSNR and SSIM metrics, where higher values indicate better results

	CycleGAN		GC-CycleGAN		SC-CycleGAN		MUNIT		DRIT++		StarGAN-v2		MGUIT		InstaFormer		HiFi-Syn	
	PSNR	SSIM	PSNR	SSIM	PSNR	SSIM	PSNR	SSIM	PSNR	SSIM	PSNR	SSIM	PSNR	SSIM	PSNR	SSIM	PSNR	SSIM
T1→T2	16.4163	0.7701	16.7513	0.7768	16.8314	0.7801	20.3364	0.8167	22.3565	0.8580	21.3841	0.7704	21.9644	0.8775	22.0187	0.8793	23.4402	0.8941
T2→T1	18.8426	0.7835	18.9146	0.7894	19.1136	0.7914	19.5421	0.8058	24.9558	0.8790	21.9111	0.7821	25.6549	0.8922	25.7539	0.8916	25.7228	0.9078
T1→T1ce	22.3416	0.7952	22.3140	0.7943	22.8474	0.8005	22.0965	0.7531	19.0562	0.7914	21.9245	0.8294	18.9326	0.8180	22.1915	0.8204	25.6167	0.8551
T1ce→T1	23.9831	0.8130	23.8754	0.8114	24.1542	0.8155	23.6318	0.7736	26.0656	0.8758	23.1861	0.8464	26.1800	0.8765	24.9027	0.8672	26.8424	0.8973
T1→Flair	16.3494	0.7458	16.4155	0.7512	16.7621	0.7548	21.6752	0.7670	18.9193	0.7709	19.1493	0.7592	19.4815	0.7772	20.2528	0.7864	21.3512	0.8061
Flair→T1	20.4216	0.7878	20.4481	0.7910	20.5253	0.7934	20.6847	0.7569	24.4028	0.8614	21.4930	0.7736	23.2653	0.8231	24.7532	0.8671	26.0135	0.8836
Average	19.8924	0.7826	19.7865	0.7857	20.0390	0.7893	21.3278	0.7789	22.6260	0.8394	21.5564	0.7935	22.5798	0.8441	23.3121	0.8520	24.8311	0.8740

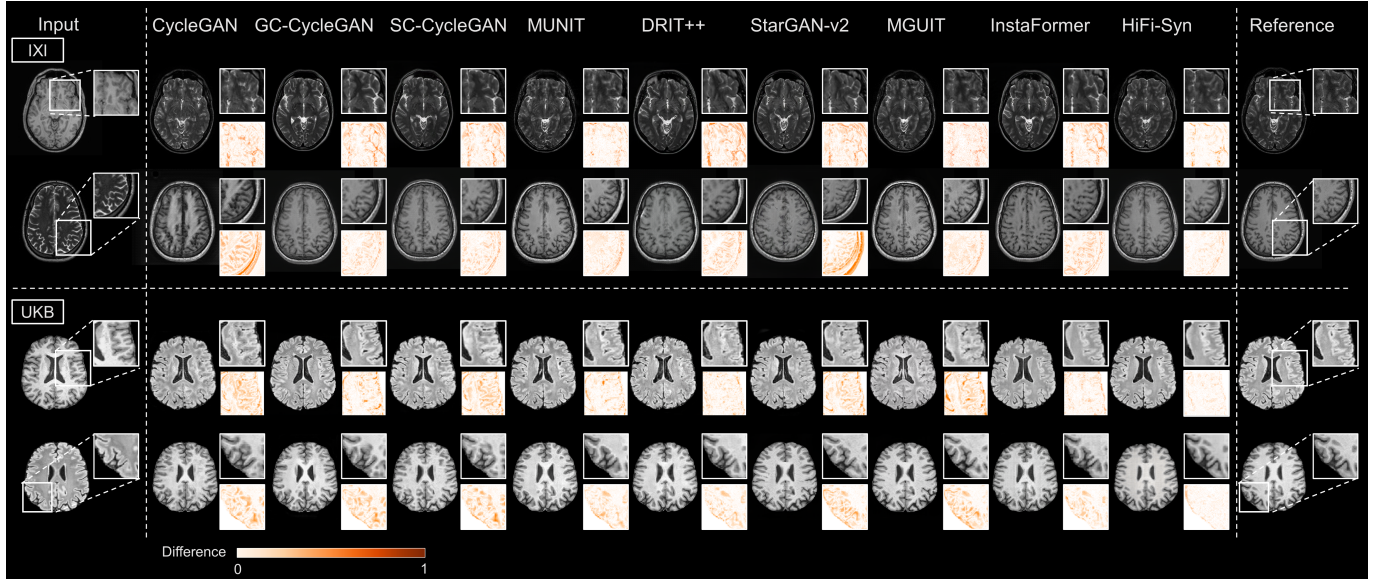


Fig. 4. Comparison of I2I translation methods on the IXI and UKB datasets. (Top to bottom) T1→T2, T2→T1, T1→T2-Flair, and T2-Flair→T1 results. Compared to other SOTA methods, HiFi-Syn shows superior structure-preserving translation with clearer error maps.

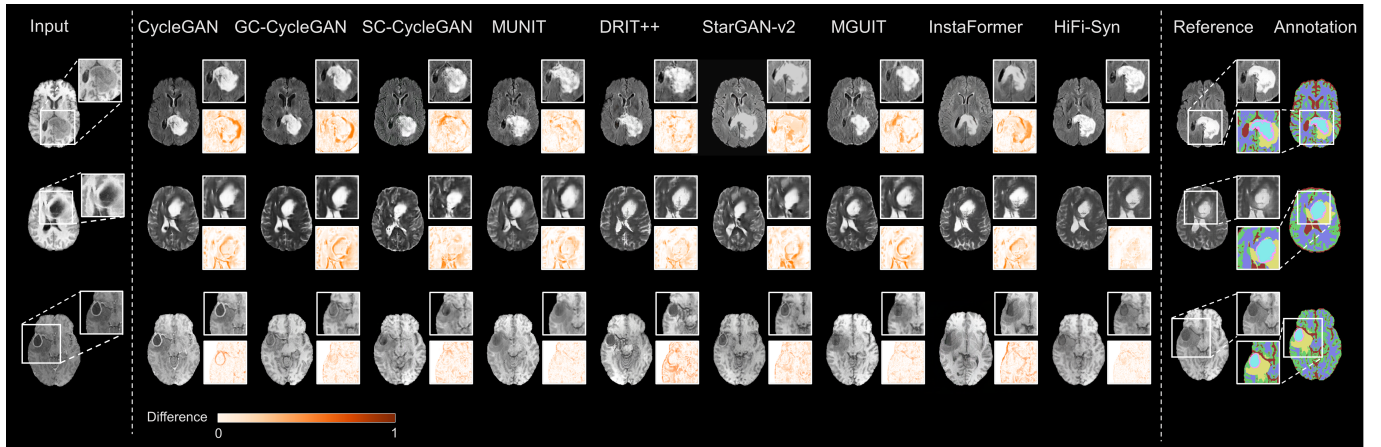


Fig. 5. Comparison of I2I translation methods on the BraTS dataset. (Top to bottom) T1→T2-Flair, T1→T2, and T1ce→T1 results. Compared to other SOTA methods, HiFi-Syn shows superior structure-preserving translation on both normal and non-normal MR images with clearer error maps. Note that annotations are unseen during testing.

consistency loss is employed to improve the accuracy of the generated images, particularly focusing on addressing challenges at the boundaries.

- **SC-CycleGAN:** This method is developed for unsupervised image synthesis, with a primary focus on preserving structural consistency between the translated images. It introduces a modality-independent neighborhood descriptor within the structure-consistency loss to emphasize the importance of structural details.

5. Results and Discussion

5.1. Quantitative Evaluation on Normal Brain Samples

We initiate our experiments with a quantitative evaluation of our proposed structure-preserving synthesis technique on normal brain images, using two datasets: IXI and UKB. By examining the results of these experiments, we aim to quantify its effectiveness in faithfully reproducing the intricate structural details present in normal brain images.

Fig. 4 shows several exemplary synthetic images of the SOTA methods on the IXI and UKB datasets. It can be observed that for both datasets, InstaFormer and StarGAN-v2 struggle to preserve the anatomical structures of gyri and sulci. This becomes particularly evident in the second example, as illustrated in Fig. 4. Although DRIT++ and MGUIT shows distinct contrast and boundaries, they are peculiarly prone to generate unrealistic anatomies in the T1 \leftrightarrow T2-Flair tasks. This is unsurprising, while they have decoupled the MR images into attribute and content spaces, they lack structure-wise guidance during translation. This absence can result in fragmented and ambiguous embedding spaces and is insufficient to ensure the preservation of fine brain structure during translation. Similarly, synthetic images obtained from CycleGAN confuse the appearances of structures across different modalities. For example, CSF of CycleGAN synthetic MRI has high contrast in T1 and low contrast in T2, which is opposite to the real MRIs. Thanks to our proposed hierarchical triple-level granularity discrimination, our synthetic images preserve structures during translation and reproduce the anatomic-specific contrast variations between multi-modality MRI. We observe the successful preservation of critical anatomical landmarks, including ventricles, sulci, and gyri. The quantitative results of PSNR and SSIM in Table 1 & 2 confirm the superiority of HiFi-Syn, which surpasses other methods in most translation tasks.

5.2. Quantitative Evaluation on Tumor-Bearing Samples

Non-normal structures, specifically referring to tumors in our study, exhibit varying contrasts across different imaging modalities due to their pathological characteristics. These non-normal structures hold significant pathological implications, prompting us to conduct further evaluations. In particular, we assessed the network’s capacity to accurately retain the structural characteristics of normal tissues while simultaneously deciphering the anatomical features of non-normal tissues. Therefore, in this subsection, we present evaluations conducted on the BraTS dataset.

The PSNR and SSIM metrics are listed in the Table 3. We can observe that HiFi-Syn exhibits a substantial lead over other methods, and this advantage becomes even more pronounced when compared to the advantages observed in previous normal brain datasets. This enhanced performance is likely attributed to the intricate semantic information inherent in tumor-bearing images, which may pose difficulties for other methods in discerning various structures. The instance-level I2I network, InstaFormer and MGUIT, achieved results within the second tier. These methods, in contrast to those exclusively concentrating on global content, take into account instance-level representations, which can capture more detailed and local information. However, the challenges lie in the granularity of instance-level learning, which can struggle to effectively handle complex anatomical structures. This limitation becomes evident in scenarios where intricate structures and fine-grained details require a more nuanced comprehension, potentially contributing to their placement in the second tier of results. Through visual inspection of the generated results shown in Fig. 5, we find that InstaFormer and other baselines introduce varying degrees of

Table 4. Quantitative results for FSL (Jenkinson et al., 2012) segmentation using synthetic T1 image. We report per-class Dice score and volumetric similarity results for the T2 \rightarrow T1 case via voxel-based analysis

Method	T2 \rightarrow T1			
	GM Dice	GM VS	WM Dice	WM VS
CycleGAN (Zhu et al., 2017)	85.5	95.7	85.9	95.7
GC-CycleGAN (Hiasa et al., 2018)	85.7	95.9	86.1	89.2
SC-CycleGAN (Yang et al., 2020)	86.1	96.3	86.4	89.6
MGUIT (Jeong et al., 2021)	89.2	97.2	87.5	97.0
MUNIT (Huang et al., 2018)	86.4	96.7	87.0	96.1
DRIT++ (Lee et al., 2020)	87.3	94.1	88.3	96.6
StarGAN-v2 (Choi et al., 2020)	86.2	95.5	84.9	96.2
InstaFormer (Kim et al., 2022)	89.3	96.6	88.6	97.1
HiFi-Syn	89.9	97.5	90.3	98.3

distortion in the tumor regions, potentially compromise downstream tasks.

Furthermore, we conducted an expert study to evaluate the synthesized images generated by different methods. We randomly selected 18 subjects from BraTS test set, encompassing a total of 162 images that underwent evaluation by 6 experts for their structural preservation and diagnostic value. As shown in Fig. 6, HiFi-Syn surpasses others with a significant margin for both metrics.

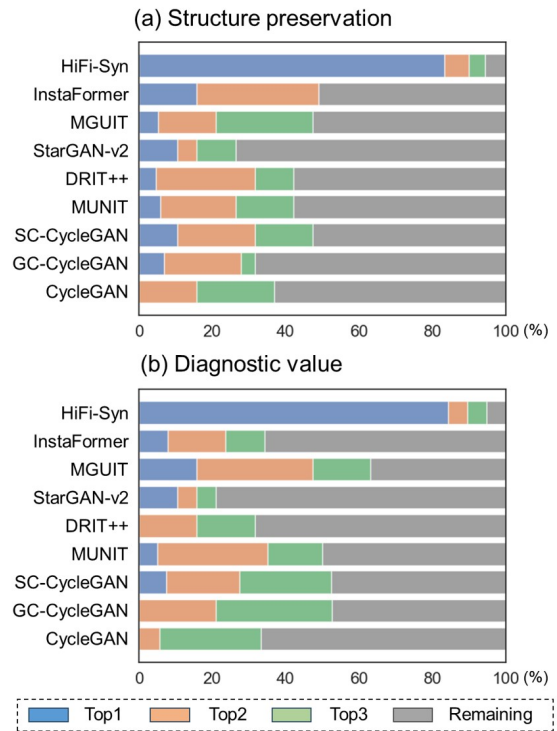


Fig. 6. Expert evaluation results on BraTS dataset. In terms of structural preservation and diagnostic value, HiFi-Syn is scored as the best method for tumor-bearing samples. Experts were allowed to provide tied rankings to different methods.

5.3. Voxel-Level Analysis

5.3.1. Following the voxel-based analysis Paradigm

Structural mismatches, such as those involving gray or white matter, can result in misdiagnosis or the identification of unreliable biomarkers in neuroimaging downstream tasks. Inspired by the voxel-based analysis paradigm (Ashburner and Friston,

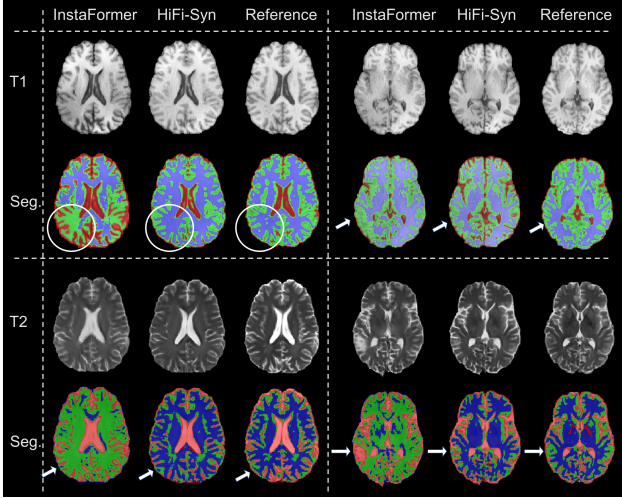


Fig. 7. Synthesis evaluation through downstream segmentation tasks. Compared to InstaFormer (the best SOTA method), the synthetic images from HiFi-Syn retain minimal mismatches in downstream tasks (Green: GM; Blue: WM; Red: CSF). The arrows and circles in white color indicate some representative regions.

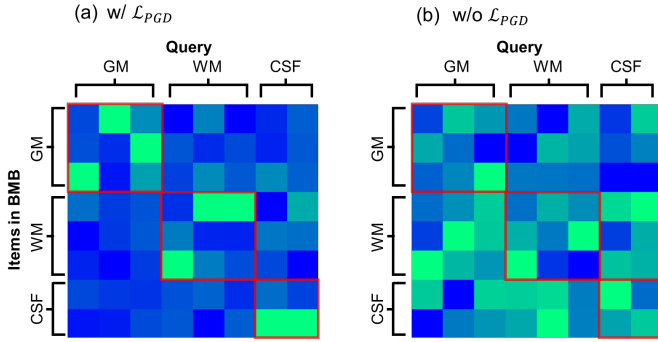


Fig. 8. Visualization of affine scores in eq. (1). (Left) learned w/ and (right) w/o \mathcal{L}_{PGD} . The red box represents reasonable matches between the query and the items (blue: low; green: high). For better visualization, eight randomly selected queries and items from GM, WM, and CSF trained on IXI dataset are involved.

2000), we first segment our synthesized image into gray/white matter using FSL FAST (Jenkinson et al., 2012), to assess the amount of the anatomical information transferred by HiFi-Syn from the real image. The results, presented in Fig. 7 and Table 4, show that our results are consistently better than other methods, including InstaFormer (Kim et al., 2022), as measured by Dice scores and volume similarity (VS) that quantify the overlap of structures between synthetic and real images.

5.3.2. Data Augmentation for Segmentation on IXI Dataset

We further investigate the impact of image synthesis for data augmentation purpose. For this experiment, we also compare the improvement achieved with recent SOTA generation methods in Table 5. As the results revealed, HiFi-Syn used as a data augmentation trick could utilize unpaired data from medical images and increase the heterogeneity of the training dataset.

Table 5. Improvement comparison on IXI segmentation with different image synthetic methods

T1 testing (%)	GM	WM	CSF	Avg.
Real	94.3	95.1	96.2	95.2
+Syn. (InstaFormer (Kim et al., 2022))	94.6	95.5	96.4	95.5
+Syn. (HiFi-Syn)	94.9	95.8	96.5	95.7
T2 testing (%)	GM	WM	CSF	Avg.
Real	77.6	83.9	87.8	83.1
+Syn. (InstaFormer (Kim et al., 2022))	78.0	84.3	88.1	83.5
+Syn. (HiFi-Syn)	78.5	84.6	88.3	83.8

Table 6. Quantitative comparison for variants of MedSyn-HDR. We measure the average PSNR and SSIM on IXI dataset. *, **: setting (i) and (ii) detailed in Sec. 5.4.1, respectively

Task	\mathcal{L}_{PGD}	\mathcal{L}_{SGD}	\mathcal{L}_{GGD}	PSNR	SSIM
T1 \rightarrow T2			*	22.1558	0.7975
	**			22.1682	0.8041
	✓			22.7219	0.8096
	✓	✓		23.4156	0.8174
	✓	✓		23.8073	0.8212
	✓	✓	✓	23.8376	0.8240
T2 \rightarrow T1			*	22.5482	0.8131
	**			22.6818	0.8164
	✓			22.9082	0.8247
	✓	✓		23.4603	0.8279
	✓	✓		23.6274	0.8347
	✓	✓	✓	24.1751	0.8371

5.4. Ablation Study

In this subsection, we investigate how hierarchical granularity discrimination improves translation performance. We present the following experiment results and analyses from three aspects, the impact of three discrimination strategies, visualization of memory items from BMB as well as latent content feature distribution.

5.4.1. Impact of Discrimination Strategies

We define our framework w/o the Brain Memory Bank (BMB) as the baseline model and explore the impact of 1) w/ global-level granularity discrimination loss \mathcal{L}_{GGD} ; 2) w/ structure-level granularity discrimination loss \mathcal{L}_{SGD} ; 3) w/ pixel-level granularity discrimination \mathcal{L}_{PGD} . As for the memory setting of BMB, we compare (i) w/ only global memory items in BMB and in the absence of structure categories and (ii) w/ both global and structure-wise items. We execute ablation study on IXI dataset, which is suitable to demonstrate the efficiency of individual units. The quantitative results are shown in Table 6. We can observe that the setting (ii) w/ $\mathcal{L}_{PGD,SGD}$ achieves significant improvement as structural constraints imposed to network. Compared with (ii) and (i), it also illustrates that structure-wise memory items are necessary for learning differentiating representations. It is also worth noting that the introduction of these modules does not significantly increase our model's time complexity.

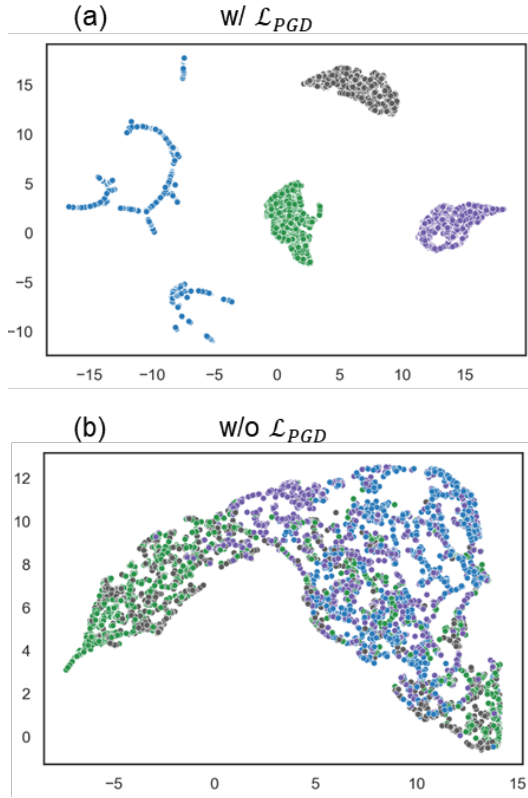


Fig. 9. Visualization of attribute space distribution by UMAP (McInnes et al., 2018). (Left) w/ and (right) w/o \mathcal{L}_{PGD} (green: GM; grey: WM; purple: CSF, blue: background).

5.4.2. BMB Items and Feature Distribution

We notice that there is a performance deterioration when \mathcal{L}_{PGD} is not used in (ii). To investigate its effects, we exhibit the affinity scores in e.q. (1) from the above-mentioned two models trained on IXI dataset. As shown in Fig. 8, it's worth noting that the queries from specific structures s_i manifest pronounced activation in corresponding memory items. This indicates that our proposed pixel-level granularity discrimination can enhance the discriminative capacity of the model and mining structure-wise knowledge during training.

We further visualize in Fig. 9 the distribution of query features from different structures in IXI dataset. We can observe that with our proposed losses, model can learned more discriminating embedded features.

One significant implication of our research is its potential utility in addressing the challenges associated with rare diseases characterized by limited available samples. As previously presented in the Fig. 5, HiFi-Syn could be served as a data augmentation strategy, especially in this case. By leveraging our approach, it becomes conceivable to augment the effective sample size, thereby promoting more extensive applications of deep learning, particularly when the original sample size is small. This has the potential to facilitate research into rare diseases with sparse datasets, providing a valuable contribution to this field.

Another critical aspect to consider is the absence of multi-modality in medical imaging. Collecting multi-modal data can

be resource-intensive, involving significant acquisition costs and demanding patient cooperation. Our approach, which excels in generating multi-modal images while preserving structural integrity, could mitigate some of these challenges. It offers a promising solution to resolving these concerns posed by missing modalities, making efficient use of available data resources and having the potential to reduce the logistical burden associated with multi-modal imaging protocols.

6. Conclusion

In this work, we present a hierarchical granularity discrimination strategy designed to leverage the diverse levels of semantic information present in medical images. Our model, HiFi-Syn, employs three levels of discrimination granularity, thereby ensuring anatomical consistency throughout the translation process. The experimental results demonstrate that HiFi-Syn achieves a SOTA performance across three brain MRI datasets, whether in normal or abnormal MR images. The diagnostic value of synthesized MR images containing brain tumors has been assessed by radiologists. This indicates that our model may offer an alternative solution in scenarios where specific MR modalities are unavailable. HiFi-Syn improves image translation capabilities in the context of medical imaging while preserving structural integrity during translation, providing novel insights into the field.

References

- Alpher, A., 2002. Frobnication. *Journal of Foo* 12, 234–278.
- Alpher, A., Fotheringham-Smythe, F.P.N., 2003. Frobnication revisited. *Journal of Foo* 13, 234–278.
- Alpher, A., Fotheringham-Smythe, F.P.N., Gamow, G., 2004. Can a machine frobnicate? *Journal of Foo* 14, 234–278.
- Ashburner, J., Friston, K.J., 2000. Voxel-based morphometry—the methods. *Neuroimage* 11, 805–821.
- Avants, B.B., Tustison, N., Song, G., et al., 2009. Advanced normalization tools (ants). *Insight j* 2, 1–35.
- Bhattacharjee, D., Kim, S., Vizier, G., Salzmann, M., 2020. Dunit: Detection-based unsupervised image-to-image translation, in: *Proceedings of the IEEE/CVF Conference on Computer Vision and Pattern Recognition*, pp. 4787–4796.
- Chartsias, A., Joyce, T., Papanastasiou, G., Semple, S., Williams, M., Newby, D., Dharmakumar, R., Tsaftaris, S.A., 2018. Factorised spatial representation learning: Application in semi-supervised myocardial segmentation, in: *International Conference on Medical Image Computing and Computer-Assisted Intervention*, Springer. pp. 490–498.
- Chartsias, A., Joyce, T., Papanastasiou, G., Semple, S., Williams, M., Newby, D.E., Dharmakumar, R., Tsaftaris, S.A., 2019a. Disentangled representation learning in cardiac image analysis. *Medical image analysis* 58, 101535.
- Chartsias, A., Papanastasiou, G., Wang, C., Stirrat, C., Semple, S., Newby, D., Dharmakumar, R., Tsaftaris, S.A., 2019b. Multimodal cardiac segmentation using disentangled representation learning, in: *International Workshop on Statistical Atlases and Computational Models of the Heart*, Springer. pp. 128–137.
- Chen, T., Kornblith, S., Norouzi, M., Hinton, G., 2020a. A simple framework for contrastive learning of visual representations, in: *International conference on machine learning*, PMLR. pp. 1597–1607.
- Chen, X., Fan, H., Girshick, R., He, K., 2020b. Improved baselines with momentum contrastive learning. *arXiv preprint arXiv:2003.04297*.
- Chen, X., Xie, S., He, K., 2021. An empirical study of training self-supervised vision transformers, in: *Proceedings of the IEEE/CVF International Conference on Computer Vision*, pp. 9640–9649.

- Choi, Y., Uh, Y., Yoo, J., Ha, J.W., 2020. Stargan v2: Diverse image synthesis for multiple domains, in: Proceedings of the IEEE/CVF conference on computer vision and pattern recognition, pp. 8188–8197.
- Dalmaz, O., Yurt, M., Çukur, T., 2022. Resvit: Residual vision transformers for multimodal medical image synthesis. *IEEE Transactions on Medical Imaging* 41, 2598–2614.
- Emami, H., Dong, M., Nejad-Davarani, S.P., Glide-Hurst, C.K., 2021. Sagan: Structure-aware gan for organ-preserving synthetic ct generation, in: Medical Image Computing and Computer Assisted Intervention–MICCAI 2021: 24th International Conference, Strasbourg, France, September 27–October 1, 2021, Proceedings, Part VI 24, Springer. pp. 471–481.
- Gong, D., Liu, L., Le, V., Saha, B., Mansour, M.R., Venkatesh, S., Hengel, A.v.d., 2019. Memorizing normality to detect anomaly: Memory-augmented deep autoencoder for unsupervised anomaly detection, in: Proceedings of the IEEE/CVF International Conference on Computer Vision, pp. 1705–1714.
- Guo, S., Zhou, Q., Zhou, Y., Gu, Q., Tang, J., Feng, Z., Ma, L., 2021. Label-free regional consistency for image-to-image translation, in: 2021 IEEE International Conference on Multimedia and Expo (ICME), IEEE. pp. 1–6.
- Han, X., Yu, Z., Zhuo, Y., Zhao, B., Ren, Y., Lamm, L., Xue, X., Feng, J., Marr, C., Shan, F., et al., 2022. The value of longitudinal clinical data and paired ct scans in predicting the deterioration of covid-19 revealed by an artificial intelligence system. *Iscience* 25.
- He, K., Fan, H., Wu, Y., Xie, S., Girshick, R., 2020. Momentum contrast for unsupervised visual representation learning, in: Proceedings of the IEEE/CVF conference on computer vision and pattern recognition, pp. 9729–9738.
- Hiasa, Y., Otake, Y., Takao, M., Matsuo, T., Takashima, K., Carass, A., Prince, J.L., Sugano, N., Sato, Y., 2018. Cross-modality image synthesis from unpaired data using cyclegan: Effects of gradient consistency loss and training data size, in: Simulation and Synthesis in Medical Imaging: Third International Workshop, SASHIMI 2018, Held in Conjunction with MICCAI 2018, Granada, Spain, September 16, 2018, Proceedings 3, Springer. pp. 31–41.
- Hu, H., Cui, J., Wang, L., 2021. Region-aware contrastive learning for semantic segmentation, in: Proceedings of the IEEE/CVF International Conference on Computer Vision, pp. 16291–16301.
- Huang, X., Liu, M.Y., Belongie, S., Kautz, J., 2018. Multimodal unsupervised image-to-image translation, in: Proceedings of the European conference on computer vision (ECCV), pp. 172–189.
- Imambi, S., Prakash, K.B., Kanagachidambaresan, G., 2021. Pytorch. Programming with TensorFlow: Solution for Edge Computing Applications , 87–104.
- Isensee, F., Jaeger, P.F., Kohl, S.A., Petersen, J., Maier-Hein, K.H., 2021. nnu-net: a self-configuring method for deep learning-based biomedical image segmentation. *Nature methods* 18, 203–211.
- Isensee, F., Petersen, J., Kohl, S.A., Jäger, P.F., Maier-Hein, K.H., 2019. nnu-net: Breaking the spell on successful medical image segmentation. *arXiv preprint arXiv:1904.08128* 1, 2.
- Isola, P., Zhu, J.Y., Zhou, T., Efros, A.A., 2017. Image-to-image translation with conditional adversarial networks, in: Proceedings of the IEEE conference on computer vision and pattern recognition, pp. 1125–1134.
- Jenkinson, M., Beckmann, C.F., Behrens, T.E., Woolrich, M.W., Smith, S.M., 2012. *Fsl. Neuroimage* 62, 782–790.
- Jeong, S., Kim, Y., Lee, E., Sohn, K., 2021. Memory-guided unsupervised image-to-image translation, in: Proceedings of the IEEE/CVF conference on computer vision and pattern recognition, pp. 6558–6567.
- Ji, Z., Hou, Z., Liu, X., Pang, Y., Li, X., 2023. Memorizing complementation network for few-shot class-incremental learning. *IEEE Transactions on Image Processing* .
- Kang, M., Chikontwe, P., Won, D., Luna, M., Park, S.H., 2023. Structure-preserving image translation for multi-source medical image domain adaptation. *Pattern Recognition* 144, 109840.
- Khosla, P., Teterwak, P., Wang, C., Sarna, A., Tian, Y., Isola, P., Maschinot, A., Liu, C., Krishnan, D., 2020a. Supervised contrastive learning. *Advances in neural information processing systems* 33, 18661–18673.
- Khosla, P., Teterwak, P., Wang, C., Sarna, A., Tian, Y., Isola, P., Maschinot, A., Liu, C., Krishnan, D., 2020b. Supervised contrastive learning. *Advances in neural information processing systems* 33, 18661–18673.
- Kim, S., Baek, J., Park, J., Kim, G., Kim, S., 2022. Instaformer: Instance-aware image-to-image translation with transformer, in: Proceedings of the IEEE/CVF Conference on Computer Vision and Pattern Recognition, pp. 18321–18331.
- Kim, T., Cha, M., Kim, H., Lee, J.K., Kim, J., 2017. Learning to discover cross-domain relations with generative adversarial networks, in: International conference on machine learning, PMLR. pp. 1857–1865.
- Kingma, D.P., Ba, J., 2014. Adam: A method for stochastic optimization. *arXiv preprint arXiv:1412.6980* .
- Kwon, G., Ye, J.C., 2021. Diagonal attention and style-based gan for content-style disentanglement in image generation and translation, in: Proceedings of the IEEE/CVF International Conference on Computer Vision, pp. 13980–13989.
- Lee, H.Y., Tseng, H.Y., Huang, J.B., Singh, M., Yang, M.H., 2018. Diverse image-to-image translation via disentangled representations, in: Proceedings of the European conference on computer vision (ECCV), pp. 35–51.
- Lee, H.Y., Tseng, H.Y., Mao, Q., Huang, J.B., Lu, Y.D., Singh, M., Yang, M.H., 2020. Dri++: Diverse image-to-image translation via disentangled representations. *International Journal of Computer Vision* 128, 2402–2417.
- Lee, J., Gu, J., Ye, J.C., 2021. Unsupervised ct metal artifact learning using attention-guided β -cyclegan. *IEEE Transactions on Medical Imaging* 40, 3932–3944.
- Locatello, F., Bauer, S., Lucic, M., Raetsch, G., Gelly, S., Schölkopf, B., Bachem, O., 2019a. Challenging common assumptions in the unsupervised learning of disentangled representations, in: international conference on machine learning, PMLR. pp. 4114–4124.
- Locatello, F., Tschannen, M., Bauer, S., Rätsch, G., Schölkopf, B., Bachem, O., 2019b. Disentangling factors of variation using few labels. *arXiv preprint arXiv:1905.01258* .
- Ma, Y., Liu, J., Liu, Y., Fu, H., Hu, Y., Cheng, J., Qi, H., Wu, Y., Zhang, J., Zhao, Y., 2021. Structure and illumination constrained gan for medical image enhancement. *IEEE Transactions on Medical Imaging* 40, 3955–3967.
- McInnes, L., Healy, J., Melville, J., 2018. Umap: Uniform manifold approximation and projection for dimension reduction. *arXiv preprint arXiv:1802.03426* .
- Menze, B.H., Jakab, A., Bauer, S., Kalpathy-Cramer, J., Farahani, K., Kirby, J., Burren, Y., Porz, N., Slotboom, J., Wiest, R., et al., 2014. The multimodal brain tumor image segmentation benchmark (brats). *IEEE transactions on medical imaging* 34, 1993–2024.
- Miller, K.L., Alfaro-Almagro, F., Bangerter, N.K., Thomas, D.L., Yacoub, E., Xu, J., Bartsch, A.J., Jbabdi, S., Sotiropoulos, S.N., Andersson, J.L., et al., 2016. Multimodal population brain imaging in the uk biobank prospective epidemiological study. *Nature neuroscience* 19, 1523–1536.
- Name, F.A., 2014a. The frobnicatable foo filter. Face and Gesture submission ID 324. Supplied as additional material fg324.pdf.
- Name, F.A., 2014b. Frobnication tutorial. Supplied as additional material tr.pdf.
- Özbe, M., Dalmaz, O., Dar, S.U., Bedel, H.A., Öztürk, Ş., Güngör, A., Çukur, T., 2023. Unsupervised medical image translation with adversarial diffusion models. *IEEE Transactions on Medical Imaging* .
- Park, H., Noh, J., Ham, B., 2020a. Learning memory-guided normality for anomaly detection, in: Proceedings of the IEEE/CVF conference on computer vision and pattern recognition, pp. 14372–14381.
- Park, T., Efros, A.A., Zhang, R., Zhu, J.Y., 2020b. Contrastive learning for unpaired image-to-image translation, in: Computer Vision–ECCV 2020: 16th European Conference, Glasgow, UK, August 23–28, 2020, Proceedings, Part IX 16, Springer. pp. 319–345.
- Phan, V.M.H., Liao, Z., Verjans, J.W., To, M.S., 2023. Structure-preserving synthesis: Maskgan for unpaired mr-ct translation, in: International Conference on Medical Image Computing and Computer-Assisted Intervention, Springer. pp. 56–65.
- Qasim, A.B., Ezhov, I., Shit, S., Schoppe, O., Paetzold, J.C., Sekuboyina, A., Kofler, F., Lipkova, J., Li, H., Menze, B., 2020. Red-gan: Attacking class imbalance via conditioned generation. yet another medical imaging perspective., in: Medical Imaging with Deep Learning, PMLR. pp. 655–668.
- Saini, J., Gupta, R.K., Kumar, M., Singh, A., Saha, I., Santosh, V., Beniwal, M., Kandavel, T., Cauteren, M.V., 2019. Comparative evaluation of cerebral gliomas using rcbv measurements during sequential acquisition of t1-perfusion and t2*-perfusion mri. *PLoS one* 14, e0215400.
- Shen, Z., Huang, M., Shi, J., Xue, X., Huang, T.S., 2019. Towards instance-level image-to-image translation, in: Proceedings of the IEEE/CVF conference on computer vision and pattern recognition, pp. 3683–3692.
- Shen, Z., Zhou, S.K., Chen, Y., Georgescu, B., Liu, X., Huang, T., 2020. One-to-one mapping for unpaired image-to-image translation, in: Proceedings of the IEEE/CVF Winter Conference on Applications of Computer Vision, pp. 1170–1179.

- Siddiquee, M.M.R., Zhou, Z., Tajbakhsh, N., Feng, R., Gotway, M.B., Bengio, Y., Liang, J., 2019. Learning fixed points in generative adversarial networks: From image-to-image translation to disease detection and localization, in: Proceedings of the IEEE/CVF international conference on computer vision, pp. 191–200.
- Wang, C.J., Rost, N.S., Golland, P., 2023. Spatial-intensity transforms for medical image-to-image translation. *IEEE Transactions on Medical Imaging*.
- Wang, F., Liu, H., 2021. Understanding the behaviour of contrastive loss, in: Proceedings of the IEEE/CVF conference on computer vision and pattern recognition, pp. 2495–2504.
- Weston, J., Chopra, S., Bordes, A., 2014. Memory networks. *arXiv preprint arXiv:1410.3916*.
- Yang, H., Sun, J., Carass, A., Zhao, C., Lee, J., Prince, J.L., Xu, Z., 2020. Unsupervised mr-to-ct synthesis using structure-constrained cyclegan. *IEEE transactions on medical imaging* 39, 4249–4261.
- Yi, Z., Zhang, H., Tan, P., Gong, M., 2017. Dualgan: Unsupervised dual learning for image-to-image translation, in: Proceedings of the IEEE international conference on computer vision, pp. 2849–2857.
- Yu, Z., Han, X., Xu, W., Zhang, J., Marr, C., Shen, D., Peng, T., Zhang, X.Y., Feng, J., 2022a. A generalizable brain extraction net (ben) for multimodal mri data from rodents, nonhuman primates, and humans. *Elife* 11, e81217.
- Yu, Z., Han, X., Zhang, S., Feng, J., Peng, T., Zhang, X.Y., 2022b. Mousegan++: Unsupervised disentanglement and contrastive representation for multiple mri modalities synthesis and structural segmentation of mouse brain. *IEEE Transactions on Medical Imaging* 42, 1197–1209.
- Yu, Z., Zhai, Y., Han, X., Peng, T., Zhang, X.Y., 2021. Mousegan: Gan-based multiple mri modalities synthesis and segmentation for mouse brain structures, in: Medical Image Computing and Computer Assisted Intervention–MICCAI 2021: 24th International Conference, Strasbourg, France, September 27–October 1, 2021, Proceedings, Part I 24, Springer. pp. 442–450.
- Yu, Z., Zhao, B., Zhang, Y., Zhang, S., Chen, X., Yang, H., Peng, T., Zhang, X.Y., 2023. Cross-grained contrastive representation for unsupervised lesion segmentation in medical images, in: Proceedings of the IEEE/CVF International Conference on Computer Vision, pp. 2347–2354.
- Yushkevich, P.A., Gao, Y., Gerig, G., 2016. Itk-snap: An interactive tool for semi-automatic segmentation of multi-modality biomedical images, in: 2016 38th annual international conference of the IEEE engineering in medicine and biology society (EMBC), IEEE. pp. 3342–3345.
- Zhang, S., Chen, X., Shen, X., Ren, B., Yu, Z., Yang, H., Jiang, X., Shen, D., Zhou, Y., Zhang, X.Y., 2023. A-gcl: Adversarial graph contrastive learning for fmri analysis to diagnose neurodevelopmental disorders. *Medical Image Analysis* 90, 102932.
- Zhang, Y., Tang, F., Dong, W., Huang, H., Ma, C., Lee, T.Y., Xu, C., 2022. Domain enhanced arbitrary image style transfer via contrastive learning, in: ACM SIGGRAPH 2022 Conference Proceedings, pp. 1–8.
- Zhu, J.Y., Park, T., Isola, P., Efros, A.A., 2017. Unpaired image-to-image translation using cycle-consistent adversarial networks, in: Proceedings of the IEEE international conference on computer vision, pp. 2223–2232.